Effects of Synthesis Parameters on the Crystallization and Morphological Profiles of SAPO-5 Templated by 1-Benzyl-2,3dimethyl-1H-imidazol-3-ium Hydroxide

Ismail Alhassan Auwal, Florent Dubray, Ka-Lun Wong, Fitri Khoerunnisa, Tau Chuan Ling, Svetlana Mintova, Eng-Poh Ng

Effects of Synthesis Parameters on the Crystallization and Morphological Profiles of SAPO-5 Templated by 1-Benzyl-2,3-dimethyl-1H-imidazol-3-ium Hydroxide

Ismail Alhassan Auwal,[1,2] Florent Dubray,[3] Ka-Lun Wong,[4,5] Fitri Khoerunnisa,[6] Tau Chuan Ling,[7] Svetlana Mintova,[3] Eng-Poh Ng[1*]

[1]*School of Chemical Sciences, Universiti Sains Malaysia, 11800 USM, Penang, Malaysia.*

[2]*Chemistry Department, Faculty of Natural and Applied Sciences, Sule Lamido University, PMB 048 Kafin Hausa, Jigawa State, Nigeria.*

[3]*Normandie Université, ENSICAEN, UNICAEN, CNRS, Laboratoire Catalyse et Spectrochimie, 14000, Caen, France.*

[4]*School of Energy and Chemical Engineering, Xiamen University Malaysia, 43900 Sepang, Selangor, Malaysia.*

[5]*College of Chemistry and Chemical Engineering, Xiamen University, Xiamen 361005, China.*

[6]*Department of Chemistry, Universitas Pendidikan Indonesia, Setiabudi 229, Bandung-40154, West Java, Indonesia.*

[7]*Institute of Biological Sciences, Faculty of Science, University of Malaya, 50603 Kuala Lumpur, Malaysia.*

*Corresponding author: epng@usm.my (EPN)

Abstract

The formation of SAPO-5 molecular sieves is investigated under hydrothermal conditions and templated by a new structure-directing agent, 1-benzyl-2,3-dimethyl-1H-imidazol-3-ium hydroxide ([Bzm]OH). The synthesis was carried out by tuning the synthesis parameters, *viz.* crystallization temperature, heating time and reactants molar composition (SiO_2, Al_2O_3, P_2O_5, $[Bzm]^+$, H_2O) so as to study the roles of each synthesis parameter towards the formation of SAPO-5. The results showed that these synthesis parameters had significant influences on the entire crystallization process (induction, nucleation, crystal growth, and Ostwald ripening) and physicochemical properties of SAPO-5 (morphology and crystal size). Moreover, this study also demonstrated a fast hydrothermal synthesis approach where SAPO-5 molecular sieve with hexagonal prism morphology could be crystallized within 10 h instead of days using novel [Bzm]OH heterocyclic template thus offering an alternative route for synthesizing zeolite-like materials for advanced applications.

Keywords: SAPO-5; Zeolite; Hydrothermal condition; 1-Benzyl-2,3-dimethyl-1H-imidazol-3-ium hydroxide; Crystallization process

Introduction

Aluminophosphate (AlPO-*n*) and silicoaluminophosphate (SAPO-*n*) microporous materials are a class of zeolites that are commonly utilized in industries involving adsorption, catalysis and separation processes [1, 2]. Typically, SAPO-5 is among the most important

zeotype materials due to its mild acid strength, unidimensional pore channel system, and large pore mouth opening (0.73×0.73 nm^2) [3].

SAPO-5 can be readily crystallized under hydrothermal conditions at 180–200 °C for 1–3 days with an aid of alkylamine organotemplates, e.g. triethylamine, tripropylamine, tetraethylammonium hydroxide, tetrabutylammonium hydroxide, and *N*-methyldicyclohexylamine [4-8]. The use of so-called structure-directing agents (SDAs) with different molecular shapes, sizes, and polarities have found to form SAPO-5 crystals with different morphological and physicochemical properties [9, 10].

Recently, imidazolium compounds have been explored as novel SDAs in the synthesis of AFI-type microporous solids (AlPO-5 and SAPO-5) [11, 12]. Unlike aliphatic amines, the delocalized π electrons in their cyclic ring together with their bulkier molecules create a versatile platform for adding functional properties and chemical modifications, thus altering the overall crystallization process of SAPO-5 materials [13, 14]. Besides SDAs, the crystallization process of SAPO-5 might also be affected by the synthesis parameters, particularly crystallization time, heating temperature, synthesis technique, amount and source of reactants, solvent, and aging [15]. Nevertheless, the knowledge about the impacts of those synthesis parameters on the crystallization and morphology of SAPO-5 templated by imidazolium SDA are still not well understood, and thus it is worth of further investigation.

Herein, the crystallization and morphological profiles of SAPO-5 templated by 1-benzyl-2,3-dimethyl-1H-imidazol-3-ium hydroxide as novel SDA is studied by carefully controlling the synthesis parameters. The formation mechanism of SAPO-5 is then proposed based on the X-ray diffraction and microscopy data obtained.

Experimental

Preparation of 1-benzyl-2,3-dimethyl-1H-imidazol-3-ium chloride ionic salt, [Bzm]Cl

Typically, a mixture containing 1,2-dimethylimidazole (29.98 g, 98%, Merck), benzyl chloride (66.00 g, 99%, Merck) and ethyl alcohol (30.00 g, 99%, Merck) was heated under reflux for 7 h at 100 ^{o}C under stirring. The shiny white crystalline solid formed was then purified with acetone several times before it was dried at 100 ^{o}C. The resulting product was [Bzm]Cl with a solid yield of 87.09% (Scheme 1). ^{1}H NMR (400 MHz, D_2O): δ = 2.47 ppm (3H, singlet, N-C(C*H*$_3$)-N), 3.71 (3H, singlet, N-C*H*$_3$), 5.27 (2H, singlet, N-C*H*$_2$-C_6H_5), 7.21 (1H, doublet, *J* = 3 Hz, N-C*H*=CH-N), 7.25 (1H, doublet, *J* = 3 Hz, N-CH=C*H*-N), 7.27-7.42 (5H, aromatic Ph-H). FTIR (cm^{-1}, KBr): 3074 (=C–H stretching), 2948 (C–H stretching), 1598 and 1452 (C=C), 1020 (C–N), 1536 (C=N). Anal. cacld for $C_{12}ClH_{15}N_2$: C, 64.65%; H, 6.74%; N, 12.57%; Cl, 15.94%; experimental: C, 65.02%; H, 6.67%; N, 11.54%; Cl, 16.78%.

Preparation of 1-benzyl-2,3-dimethyl-1H-imidazol-3-ium hydroxide ([Bzm]OH)

[Bzm]OH template solution was obtained *via* ion exchange of [Bzm]Cl with hydroxide resin (Amberlite® IRN-78, Sigma-Aldrich). The resultant solution was recovered by filtration before titrating with HCl solution (0.10 M) where 90% of OH^- exchange was attained. The hydroxide solution was then concentrated until 33.0% by mass at 50 °C before it was further used for SAPO-5 synthesis.

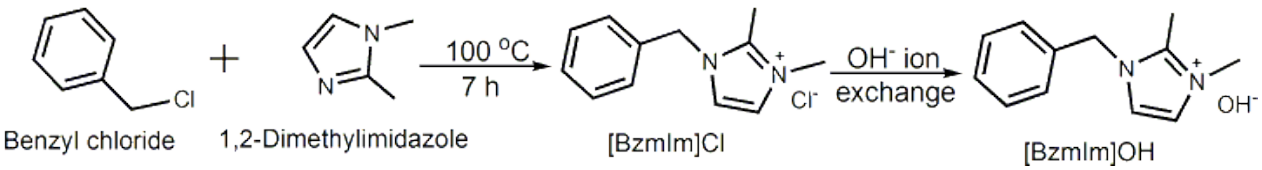

Scheme 1. Synthesis pathway of [Bzm]Cl before converting to [Bzm]OH *via* ion-exchange.

Synthesis of SAPO-5 microporous solids

SAPO-5 was synthesized as below: Firstly, aluminum isopropoxide (3.2260g, 98%, Acros) and [Bzm]OH solution (26.2753 g) were added into distilled water (5.8279 g) and stirred (500 rpm) for 35 min. Then, H_3PO_4 (4.4615 g, 85%, Merck) was slowly added dropwise over about 10 min. HS-40 colloidal silicate (0.5464 g, Sigma-Aldrich) was successively introduced forming a precursor having a molar ratio of $1Al_2O_3$:$2.5P_2O_5$:$2.5[Bzm]_2O$:$180H_2O$:$0.47SiO_2$. The resulting precursor was loaded into a Teflon lined autoclave (50 mL) and hydrothermally treated at 150 °C for 10 h. After cooling, the solid product, denoted as SH-4, was centrifuged (8000 rpm, 10 min) and washed with distilled water until pH 7 prior to freeze-drying. To study of the effects of synthesis variables, similar procedure was applied where the chemical composition of precursor hydrogels (SH1–SH20) and their respective synthesis conditions were summarized in Table 1.

Characterization

Crystallinity and phase composition of a solid were analyzed using a Bruker Advance D8 XRD diffractometer with Cu Kα X-ray source (λ = 0.15418 nm, step size = 0.02°, scanning rate = 0.2 °/min) operated at 40 kV and 10 mA. The morphological study of samples was performed with a Leo Supra 50VP electron microscope (FESEM) acquired at 30 kV. The particle size

distribution of samples was analyzed and plotted with the ImageJ (1.8.0_172) freeware by selecting 100 particles of the FESEM micrographs recorded from different spots.

Results and discussion

Effect of crystallization time

SH1, SH2, SH3, SH4, and SH5 samples with a composition of $1Al_2O_3$:$2.5P_2O_5$:$2.5[Bzm]_2O$:$180H_2O$:$0.47SiO_2$ were heated at 150 °C for 2, 4, 8, 10, and 14 h, respectively (Table 1). According to XRD analysis, the SH1 and SH2 samples were amorphous with an amorphous hump observed at 2θ = 25°–35° by the second sample indicating the phase reorganization between amorphous particles, forming secondary and more reactive amorphous entity (Fig. 1) [16]. When the duration was prolonged to 8 h, the XRD peaks due to SAPO-5 started to appear at 2θ = 7.3^o [100], 14.8° [200], 19.6° [210], and 25.8° [202], revealing that SAPO-5 nuclei started to form in the amorphous bulk solid [17]. After 10 h of heating, the amorphous solid was fully converted into crystalline SAPO-5 solid and further crystal growth of SAPO-5 crystals was observed after 14 h as indicated by the narrower and more intense AFI XRD peaks. However, a phase transformation of SAPO-5 (AFI framework) into SAPO-41 (AFO framework) was also observed with prolonged crystallization time. The XRD analysis thus demonstrated that the formation evolution of SAPO-5 underwent four distinctive stages, namely induction, nucleation, crystallization and Ostwald ripening which will be described in detail in Section 3.7.

The FESEM images of SH1, SH3, SH4 and SH5 were also captured to study the crystallization process of SAPO-5. SH1 was formed by the agglomerated and irregular-shaped

particles confirming the amorphous character of this solid (Fig. 2A(a)). The particle size distribution of SH1 was plotted and a monomodal curve centered at 120 nm was obtained (Fig. 2B(a)). This peak was shifted to larger particle sizes after 8 h indicating amorphous phase re-organization as proven by the XRD analysis (Fig. 2B(b)). In addition, another PSD centered at 500 nm was also observed, thus showing the presence of two different phases in SH3 sample. As seen, SH3 sample was a semi-crystalline solid with the SAPO-5 crystals of hexagonal prism shape were growing on the amorphous entities (Fig. 2A(b)). At 10 h, the small amorphous solids disappeared, and the SAPO-5 crystals grew further (mean size: 650 nm) as confirmed by the FESEM and PSD studies (Fig. 2A(c), 2B(c)). Successive phase transformation of SAPO-5 into SAPO-41 was also observed in SH5 after 14 h of heating where larger secondary particles made by agglomerated primary crystals of SAPO-5 and SAPO-41 (both in hexagonal prism shape [18, 19]) were detected (Fig. 2A(d), 2B(d)).

Effect of P_2O_5/Al_2O_3 molar ratio

P_2O_5 and Al_2O_3 are the basic elements for building the AFI framework. Hence, the effects of P_2O_5/Al_2O_3 ratio on the crystallization of SAPO-5 were studied using a precursor hydrogel of $1Al_2O_3$:wP_2O_5:$2.5[Bzm]_2O$:$180H_2O$:$0.47SiO_2$, where w varied from 2.0 to 3.5. When w = 2.0 (SH6), no solid was precipitated after hydrothermal treatment at 150 ^oC for 10 h which could be explained by the high alkalinity of the hydrogel (pH 10.2) as the amount of H_3PO_4 added was much lower than that of alkaline [Bzm]OH introduced. Hence, the solid product formed tended to re-dissolve back into the mother liquor [20]. When the P_2O_5/Al_2O_3 ratio increased to w = 2.5 (SH4), the alkalinity of the reaction mixture reduced significantly to nearly neutral (pH 7.5) and a solid product was successfully precipitated. The solid was found to be SAPO-5 crystalline solid

based on the XRD observation (Fig. 3). In addition, the SAPO-5 solids exhibited hexagonal prism shape with an average crystal size of 650 nm (Fig. 4A(a) and 4B(a)).

Further increasing the P_2O_5/Al_2O_3 ratio to w = 3 induced crystal growth where it could be confirmed by the narrower and more intense XRD peaks in HS7 solid. The XRD observation was also in agreement with the FESEM analysis whereby large spherical particles formed by intergrown SAPO-5 crystals were captured (Fig. 4B(b)). Meanwhile, partial phase transformation of SAPO-5 into dense cristobalite phase was observed with further increasing the P_2O_5/Al_2O_3 ratio (w = 3.5, pH 4.8), where an evolution change of morphology to intergrown grain secondary particles was also detected (Fig. 3 and 4). Obviously, an increase in P_2O_5 content had a profound effect on the crystallization profile of SAPO-5 [21].

Effect of $[Bzm]_2O/P_2O_5$ molar ratio

An equimolar amount of $[Bzm]_2O$ and P_2O_5 (x) was used to control the pH of precursor hydrogel since the crystallization of SAPO-5 is more favorable at nearly neutral pH condition as observed in Section 3.2. The pH values of the hydrogels of SH9 (x = 1.5), SH10 (x = 2.0), SH4 (x = 2.5) and SH11 (x = 3.0) were measured to be 6.42, 6.15, 6.07 and 6.14, respectively. As seen, all samples successfully produced SAPO-5 crystalline phase with no impurity but with different XRD peak widths, suggesting different crystal sizes (Fig. 5). This could also be confirmed by the PSD analysis that the mean crystals size was reduced from 1.5 µm to 1.1 µm, 650 nm and 380 nm when the x value increased from 1.5 to 2.0, 2.5 and 3.0, respectively (Fig. 6B). Furthermore, the morphology of SAPO-5 crystals was also changed from hexagonal plate shape to hexagonal prism form when increasing the x values (Fig. 6A).

It is known that the crystal size of zeolites can be predetermined from the extent of nuclei present in the precusor hydrogel. On account of this, an increase in the alkalinity of the hydrogel during the addition of a large amount of organic template, followed by adding H_3PO_4 to reach nearly neutral pH, promotes low polymerization of aluminate, phosphate and silicate species. As a result, large amount of nuclei is formed under supersaturation condition [14, 22, 23]. For this reason, small-sized SAPO-5 crystals are produced when the *x* value increases.

Effect of H_2O content

The concentration of reactants in the precursor is governed by the amount of water added which affects the properties of the final solid product (e.g. phase purity, crystallinity, size, morphology) [24]. In respect to this, four samples of different water contents (SH12, SH4, SH13 and SH14) were prepared by heating the precursor hydrogels having a molar ratio of $1Al_2O_3$:$2.5P_2O_5$:$2.5[Bzm]_2O$:yH_2O:$0.47SiO_2$ (y = 135, 180, 225 and 270) at 150 °C for 10 h, respectively. It was observed that both the crystallinity, crystal size, and purity of SAPO-5 could be controlled by simply tuning the water content. The SH12, which contained the lowest amount of water (y = 135), showed very weak XRD peaks of AFI phase at $2\theta = 12.89^o$ [110], 20.83^o [002], 25.90^o [220], and 29.00^o [311] (Fig. 7a). Thus, the sample was a semi-crystalline nano-solid (mean size of 141 nm) with a non-distinctive shape (Fig. 8A(a) and 8B(a)). The crystallinity of SAPO-5 increased when the water content was increased to y = 180 (SH4, Fig. 7b). No amorphous solid was detected under microscopy investigation. Instead, it contained crystals with hexagonal prism shape (mean size of 650 nm), *viz.* a typical morphological feature for an AFI-type material (Fig. 8A(b) and 8B(b)) [9, 25]. The crystallinity and crystal size further increased when the water contents were increased to y = 225 and 270 where co-crystallization of

tridymite as minor dense phase was observed in the latter sample (Fig. 7 and 8A). Furthermore, the SAPO-5 crystals with distinguished bimodal size distribution were also shown indicating the important role of water in the crystallization of SAPO-5 (Fig. 8B(d)).

It is known that the supersaturation condition favors the formation of a large number of nuclei when the water content is reduced. Concurrently, the enhanced alkalinity of the precursor hydrogel induces low polymerization of aluminate, phosphate and silicate species, thus resulting in the formation of smaller SAPO-5 particles [26, 27]. However, a less concentrated hydrogel with more acidic environment is prepared when increasing the water content, and it tends to retard the nucleation process and this leads to the formation of larger-sized SAPO-5 crystals [28]. Furthermore, tridymite is also co-crystallized when increasing the water content because dense crystalline phases preferably crystallize under an acidic environment [29].

Effect of SiO_2/Al_2O_3 molar ratio

In this study, the effects of silica content (expressed in SiO_2/Al_2O_3 molar ratio) were studied considering the significance and high tendency of silicon atoms insertion into the parent AlPO-5 during the crystallization process [30, 31]. Hence, the hydrogels with a composition of $1Al_2O_3{:}2.5P_2O_5{:}2.5[Bzm]_2O{:}180H_2O{:}zSiO_2$, where z = 0 (SH15), 0.23 (SH16), 0.47 (SH4) and 0.70 (SH17), were prepared. Without adding any SiO_2, the so-called AlPO-5 sample (SH15) showed an XRD pattern that perfectly matched with the AFI structure (Fig. 9a). The diffraction bands were broad suggesting small crystal size and it could be confirmed from the FESEM image that showed secondary micron-sized particles with layered morphology formed by agglomerated nanocrystals (mean size of 170 nm) (Fig. 10A(a) and 10B(a)). The phase purity remains the same when the Si content was increased to z = 0.23, 0.47, and 0.7, but a significant

change in crystal size and morphology was observed (Fig. 10A(b-d)). As seen, the SAPO-5 crystals tended to grow in *c*-direction when more Si atoms were incorporated forming hexagonal prism crystals with an elongated shape and intergrown structure. As a result, the mean particle size of SAPO-5 increased from 260 nm (z = 0.23) to 650 nm (z = 0.47) before reaching to 4.2 µm (z = 0.7) (10B(b-d)).

Effect of heating temperature

The synthesis temperature affects the crystallization process of zeolite materials since it provides the energy needed for nucleation and crystal growth [24, 32]. Hence, the hydrogel of a molar ratio of $1Al_2O_3$:$2.5P_2O_5$:$2.5[Bzm]_2O$:$180H_2O$:$0.47SiO_2$ was hydrothermally heated at 100, 120, 150 and 200 °C for 10 h (Table 5.1). The SH18 sample heated at 100 °C yielded an amorphous solid (mean size of 120 nm) with a non-distinctive shape (Fig. 11a, 12A(a) and 12B(a)). Thus, it revealed that the rate of crystallization of SAPO-5 is slow at 100 °C due to insufficient energy supplied to the system [22]. Increasing the temperature to 120 °C slightly accelerated the crystallization rate but the solid was partially converted to SAPO-5 as an amorphous hump was still observed at $2\theta = 20^o–30^o$ (Fig. 11b). On the other hand, the morphology of the solids changed to a relatively hexagonal shape having a mean size of 374 nm (Fig. 12A(b) and 12B(b)). At 150 °C, fully crystalline SAPO-5 was obtained (Fig. 11c, Fig. 12A(c)). Thus, this indicated that the crystallization of SAPO-5 is a thermally activated process that requires energy to convert amorphous precursors into crystalline solids. Nevertheless, supplying excessive energy by increasing the temperature to 200 °C led to the crystallization of a tridymite dense phase. This is because SAPO-5 is a metastable crystalline phase and it tends to transform into a denser phase at very high temperatures [33].

Formation pathway of SAPO-5 crystals

In general, the formation of SAPO-5 crystals templated by [Bzm]OH organic template involves four successive stages, namely induction, nucleation, crystal growth, and Ostwald ripening (Fig. 13). At the induction stage. Al_2O_3, P_2O_5, and SiO_2 precursors are hydrolyzed in the presence of H_2O forming low molecular-weight monomers and dimers as primary building units (Step 1) [34]. Phase reorganization also occurs when longer chain oligomers are formed *via* polycondensation as proven by the XRD analysis (Fig. 1a,b). These oligomers tend to align and enfold around the $[Bzm]^+$ molecules *via* restricted electrostatic interaction between the $[Bzm]^+$ cation and the anionic silicoaluminophosphate species forming an organic-inorganic intermediate species.

An equilibrium is established between the hydrolyzed intermediate species and the phase re-organized species, which later resulted into the nucleation stage (Step 2). During this phase, the formation of AFI framework by higher molecular-weight oligomers takes place [34]. The reaction equilibrium begins to shift to the direction of small nuclei with three-dimensional ordering so that they propagate into the eventual SAPO-5 framework structure. These nuclei serve as seeds or starting points for crystal growth in the secondary amorphous particles [35]. At this stage, the XRD and SEM measurements hardly detect the presence of SAPO-5 crystalline phase.

Further prolonging the heating time results in the complete conversion of amorphous particles into SAPO-5 crystalline solids (Step 3). This phenomenon happens due to the fact that the amorphous particles are less thermodynamically stable in the mother liquor and they tend to re-dissolve or being consumed as nutrients for further crystal growth [36].

The last stage involves Ostwald ripening where it is always experienced by large-pore zeolites due to their more opened structures and low metastability (Step 4) [37, 38]. Thus, a successive crystal phase transformation from SAPO-5 to SAPO-41 with less opened structure occurs.

The induction, nucleation, crystal growth, and Ostwald ripening are also affected by other synthesis parameters. In particular, heating temperature has the most profound effect on those stages because increasing the reaction temperature will supply more energy to the system to ease breaking and new formation of P–O–T bonds (T = Al, P, Si), and directly increasing the crystallization rate [24]. Furthermore, SAPO-5 may undergo different kinds of structural change *via* reconstructive phase transformation to a more metastable phase at high temperature. This is achieved by unit cell volume contraction through the removal of the water and/or $[Bzm]^+$ cations from the pores [22, 39]. Furthermore, the addition of SiO_2 as one of the primary building units also affects the entire crystallization process of SAPO-5. During hydrothermal treatment, the silicates compete with aluminates and phosphates in the construction of AFI framework where the former species affects the crystal growth orientation forming SAPO-5 crystals with different shapes and sizes [40].

Furthermore, the pH of precursor hydrogel has been suggested to control the nucleation rate of SAPO-5, affecting the crystal size and purity. Large and intergrown SAPO-5 crystals with co-crystallized dense phase are obtained when the crystallization occurs under acidic environments (high P_2O_5/Al_2O_3 ratio or high H_2O content) because of rapid hydrolysis and polycondensation reactions at low pH [41]. In contrast, when the crystallization takes place at nearly neutral environment (~6.0) in the excessive amount of $[Bzm]^+$ template, a supersaturation

condition is formed. It thus facilitates rapid and homogeneous nucleation rather than crystal growth, forming SAPO-5 crystals with uniform and smaller sizes [42].

Conclusion

SAPO-5 microporous solids with interesting morphologies and sizes have successfully been prepared with an aid of a novel imidazolium structure-directing agent, [Bzm]OH. In addition, the effects of the synthesis variables on the formation of SAPO-5 have also been systematically investigated. As revealed, SAPO-5 undergoes four evolutionary processes, namely induction, nucleation/propagation, crystal growth, and Ostwald ripening. Small SAPO-5 particles can be prepared under low temperature (150 °C), low water content, and concentrated template conditions where such conditions favor nucleation over crystal growth. In contrast, the high molar ratio of P_2O_5/Al_2O_3 (low pH), high SiO_2 content, long crystallization time, and high heating temperature favor the formation of big SAPO-5 crystals and in most cases, tridymite and cristobalite dense phases are also formed. Similar to aliphatic amine templates, the SAPO-5 solids crystallized using [Bzm]OH also exhibit hexagonal prism morphology. Thus, this nanoporous solid is suitable to be employed in catalysis, membrane separation, sensor, heat pump, drug carrier and adsorption technologies. Comprehensive study on studying SAPO-5 in those aspects is in progress.

Acknowledgement

This work was financially supported by RUI (1001/PKIMIA/8011128) and TETFund.

References

[1] S.F. Alam, M.-Z. Kim, Y.J. Kim, A. ur Rehman, A. Devipriyanka, P. Sharma, J.-G. Yeo, J.-S. Lee, H. Kim, C.-H. Cho, A new seeding method, dry rolling applied to synthesize SAPO-34 zeolite membrane for nitrogen/methane separation, Journal of Membrane Science, 602 (2020) 117825. https://doi.org/10.1016/j.memsci.2020.117825

[2] E.-P. Ng, H. Awala, S. Komaty, S. Mintova, Microwave-green synthesis of AlPO-n and SAPO-n (n= 5 and 18) nanosized crystals and their assembly in layers, Microporous and Mesoporous Materials, (2019 https://doi.org/10.1016/j.micromeso.2019.02.016

[3] http://www.iza-structure.org/, in, SC-IZA, 2020

[4] M. Li, C. Zeng, L. Zhang, Hydrothermal synthesis of SAPO-5 with novel morphologies from hydrogels containing acetic acid and high concentration of triethylamine under neutral or alkaline conditions, CrystEngComm, 14 (2012) 3787-3792. https://doi.org/10.1039/C2CE06645A

[5] L. Gómez-Hortigüela, J. Pérez-Pariente, F. Corà, C.R.A. Catlow, T. Blasco, Structure-directing role of molecules containing benzyl rings in the synthesis of a large-pore aluminophosphate molecular sieve: an experimental and computational study, The Journal of Physical Chemistry B, 109 (2005) 21539-21548. https://doi.org/10.1021/jp0519215

[6] F. Jiang, Z. Tang, J. Zhai, J. Ye, J. Han, Synthesis of AlPO4-5 crystals using TBAOH as template, Microporous and Mesoporous Materials, 92 (2006) 129-133. https://doi.org/10.1016/j.micromeso.2005.12.021

[7] E.-P. Ng, S.S. Sekhon, S. Mintova, Discrete MnAlPO-5 nanocrystals synthesized by an ionothermal approach, Chemical Communications, (2009) 1661-1663. https://doi.org/10.1039/B820883B

[8] R. Roldán, M. Sánchez-Sánchez, G. Sankar, F.J. Romero-Salguero, C. Jiménez-Sanchidrián, Influence of pH and Si content on Si incorporation in SAPO-5 and their catalytic activity for isomerisation of n-heptane over Pt loaded catalysts, Microporous and Mesoporous Materials, 99 (2007) 288-298. https://doi.org/10.1016/j.micromeso.2006.09.035

[9] L. Geng, H. Dong, X. Liu, B. Zhang, Efficient Manipulation of Continuous AFI-Type Aluminophosphate Membranes with Distinctive Microstructures on Macroporous α-Al_2O_3 Substrates, Molecules, 23 (2018) 1127. https://doi.org/10.3390/molecules23051127

[10] I.A. Auwal, S. Mintova, T.C. Ling, F. Khoerunnisa, K.-L. Wong, E.-P. Ng, Crystallization profile and morphological study of SAPO-5 templated by imidazolium cations of different functional groups, Microporous and Mesoporous Materials, 308 (2020) 110514. https://doi.org/10.1016/j.micromeso.2020.110514

[11] D.Y. Khoo, W.-M. Kok, R.R. Mukti, S. Mintova, E.-P. Ng, Ionothermal approach for synthesizing AlPO-5 with hexagonal thin-plate morphology influenced by various parameters at ambient pressure, Solid State Sciences, 25 (2013) 63-69. https://doi.org/10.1016/j.solidstatesciences.2013.08.008

[12] J. Feng, L. Guo, Z. Wang, B. Wang, J. Wang, T. Lu, J. Xu, Y. Zhan, A. Rawal, C. Zhao, Effect of Ionothermal Synthesis on the Acidity and Catalytic Performance of a SAPO- 5 Molecular Sieve, ChemistrySelect, 4 (2019) 10520-10524. https://doi.org/10.1002/slct.201902643

[13] E.P. Ng, L. Itani, S.S. Sekhon, S. Mintova, Micro- to Macroscopic Observations of MnAlPO- 5 Nanocrystal Growth in Ionic- Liquid Media, Chemistry–A European Journal, 16 (2010) 12890-12897. https://doi.org/10.1002/chem.201001083
[14] E.-P. Ng, K.-L. Wong, D.T.-L. Ng, H. Awala, R.R. Mukti, F. Adam, S. Mintova, AlPO-5 nanocrystals templated by 1-ethyl-2, 3-dimethylimidazolium hydroxide and their textural and water sorption properties, Materials Chemistry and Physics, 188 (2017) 49-57. https://doi.org/10.1016/j.matchemphys.2016.12.031
[15] D.Y. Khoo, H. Awala, S. Mintova, E.-P. Ng, Synthesis of AlPO-5 with diol-substituted imidazolium-based organic template, Microporous and Mesoporous Materials, 194 (2014) 200-207. https://doi.org/10.1016/j.micromeso.2014.04.010
[16] T.M.A. Ghrear, S. Rigolet, T.J. Daou, S. Mintova, T.C. Ling, S.H. Tan, E.-P. Ng, Synthesis of Cs-ABW nanozeolite in organotemplate-free system, Microporous and Mesoporous Materials, 277 (2019) 78-83. https://doi.org/10.1016/j.micromeso.2018.10.014
[17] Z. Chen, S. Zhu, P. Li, X. Li, Y. Xu, Y. Dong, W. Song, X. Yi, W. Fang, Fabricating self-assembled SAPO-5 with tailored mesoporosity and acidity using a single template, CrystEngComm, 19 (2017) 5275-5284. https://doi.org/10.1039/C7CE01132F
[18] I.A. Auwal, K.-L. Wong, T.C. Ling, B.S. Ooi, E.-P. Ng, Metal Chlorides Grafted on SAPO-5 (MClx/SAPO-5) as Reusable and Superior Catalysts for Acylation of 2-Methylfuran Under Non-Microwave Instant Heating Condition, Processes, 8 (2020) 603. https://doi.org/10.3390/pr8050603
[19] M. Agliullin, B. Kutepov, Selective Crystallization of AlPO 4-41 Molecular Sieve in the Presence of Diethylamine, Petroleum Chemistry, 60 (2020) 890-894. https://doi.org/10.1134/S0965544120080022
[20] M. Vilaseca, S. Mintova, V. Valtchev, T. Metzger, T. Bein, Synthesis of colloidal AlPO 4-18 crystals and their use for supported film growth, Journal of Materials Chemistry, 13 (2003) 1526-1528. https://doi.org/10.1039/B304670M
[21] D.S. Wragg, A.M. Slawin, R.E. Morris, The role of added water in the ionothermal synthesis of microporous aluminium phosphates, Solid State Sciences, 11 (2009) 411-416. https://doi.org/10.1016/j.solidstatesciences.2008.09.008
[22] Y. Hu, C. Liu, Y. Zhang, N. Ren, Y. Tang, Microwave-assisted hydrothermal synthesis of nanozeolites with controllable size, Microporous and Mesoporous Materials, 119 (2009) 306-314. https://doi.org/10.1016/j.micromeso.2008.11.005
[23] S.-F. Wong, K. Deekomwong, J. Wittayakun, T.C. Ling, O. Muraza, F. Adam, E.-P. Ng, Crystal growth study of KF nanozeolite and its catalytic behavior in Aldol condensation of benzaldehyde and heptanal enhanced by microwave heating, Materials Chemistry and Physics, 196 (2017) 295-301. https://doi.org/10.1016/j.matchemphys.2017.04.061
[24] S. Askari, A.B. Siahmard, R. Halladj, S.M. Alipour, Different techniques and their effective parameters in nano SAPO-34 synthesis: A review, Powder Technology, 301 (2016) 268-287. https://doi.org/10.1016/j.powtec.2016.06.018
[25] J. Chen, P. Wright, S. Natarajan, J. Thomas, Understanding the Brønsted acidity of SAPO-5, SAPO-17, SAPO-18 and SAPO-34 and their catalytic performance for methanol conversion to hydrocarbons, in: Studies in Surface Science and Catalysis, Elsevier, 1994, pp. 1731-1738. https://doi.org/10.1016/S0167-2991(08)63726-X
[26] A. Persson, B. Schoeman, J. Sterte, J.-E. Otterstedt, The synthesis of discrete colloidal particles of TPA-silicalite-1, Zeolites, 14 (1994) 557-567. https://doi.org/10.1016/0144-2449(94)90191-0

[27] T. Brar, P. France, P.G. Smirniotis, Control of crystal size and distribution of zeolite A, Industrial & Engineering Chemistry Research, 40 (2001) 1133-1139. https://doi.org/10.1021/ie000748q
[28] T. An, J. An, H. Yang, G. Li, H. Feng, X. Nie, Photocatalytic degradation kinetics and mechanism of antivirus drug-lamivudine in TiO2 dispersion, Journal of Hazardous Materials, 197 (2011) 229-236. https://doi.org/10.1016/j.jhazmat.2011.09.077
[29] S.H. Garofalini, A. Miller, Kinetics of tridymite formation, Journal of Crystal Growth, 78 (1986) 85-96. https://doi.org/10.1016/0022-0248(86)90504-X
[30] R. Wang, C. Lin, Y. Ho, L. Leu, K. Chao, Silicon species in a SAPO-5 molecular sieve, Applied Catalysis, 72 (1991) 39-49. https://doi.org/10.1016/0166-9834(91)85026-R
[31] M.W. Erichsen, S. Svelle, U. Olsbye, H-SAPO-5 as methanol-to-olefins (MTO) model catalyst: Towards elucidating the effects of acid strength, Journal of Catalysis, 298 (2013) 94-101. https://doi.org/10.1016/j.jcat.2012.11.004
[32] R. Xu, W. Pang, J. Yu, Q. Huo, J. Chen, Chemistry of zeolites and related porous materials: synthesis and structure, John Wiley & Sons, 2009.
[33] M. Briend, M. Peltre, P. Massiani, P. Man, R. Vomscheid, M. Derewinski, D. Barthomeuf, Modifications of structure and Si environment upon heating of SAPO-5, SAPO-34 and SAPO-37, in: Studies in Surface Science and Catalysis, Elsevier, 1994, pp. 613-620. https://doi.org/10.1016/S0167-2991(08)64165-8
[34] J. Grand, H. Awala, S. Mintova, Mechanism of zeolites crystal growth: new findings and open questions, CrystEngComm, 18 (2016) 650-664. https://doi.org/10.1039/C5CE02286J
[35] C.S. Cundy, P.A. Cox, The hydrothermal synthesis of zeolites: history and development from the earliest days to the present time, Chemical Reviews, 103 (2003) 663-702. https://doi.org/10.1021/cr020060i
[36] S.-F. Wong, H. Awala, A. Vincente, R. Retoux, T.C. Ling, S. Mintova, R.R. Mukti, E.-P. Ng, KF zeolite nanocrystals synthesized from organic-template-free precursor mixture, Microporous and Mesoporous Materials, 249 (2017) 105-110. https://doi.org/10.1016/j.micromeso.2017.04.053
[37] M. Jorge, S.M. Auerbach, P.A. Monson, Modeling spontaneous formation of precursor nanoparticles in clear-solution zeolite synthesis, Journal of the American Chemical Society, 127 (2005) 14388-14400. https://doi.org/10.1021/ja052402i
[38] S.M. Auerbach, M.H. Ford, P. Monson, New insights into zeolite formation from molecular modeling, Current Opinion in Colloid & Interface Science, 10 (2005) 220-225. https://doi.org/10.1016/j.cocis.2005.09.012
[39] O.D. Trong, S. Kaliaguine, Zeolite/Mesoporous Molecular Sieve Composite Materials, Nanoporous Materials: Science and Engineering, 4 (2004) 47. https://doi.org/10.1142/9781860946561_0003
[40] S.H. Jhung, J.-S. Chang, D.S. Kim, S.-E. Park, Effects of silica on the synthesis of AFI molecular sieve in acid and base conditions under microwave irradiation, Microporous and Mesoporous Materials, 71 (2004) 135-142. https://doi.org/10.1016/j.micromeso.2004.03.026
[41] C.-M. Chen, J.-M. Jehng, Effect of synthesis pH and H_2O molar ratio on the structure and morphology of aluminum phosphate (AlPO-5) molecular sieves, Catalysis Letters, 85 (2003) 73-80. https://doi.org/10.1023/A:1022120824681
[42] E.-P. Ng, S. Rigolet, T.J. Daou, S. Mintova, T.C. Ling, Micro-and macroscopic observations of the nucleation process and crystal growth of nanosized Cs-pollucite in an organotemplate-

free hydrosol, New Journal of Chemistry, 43 (2019) 17433-17440. https://doi.org/10.1039/C9NJ03151K

Figure captions

Fig. 1. XRD patterns of (a) SH1, (b) SH2, (c) SH3, (d) SH4 and (e) SH5 samples prepared using a hydrogel composition of $1Al_2O_3:2.5P_2O_5:2.5[Bzm]_2O:180H_2O:0.47SiO_2$ and heated at 150 ^oC for 2 h, 4 h, 8 h, 10 h and 14 h, respectively. Asterisks denote the presence of SAPO-41 phase.

Fig. 2. (A) FESEM images and (B) particle size distibutions of (a) SH1, (b) SH3, (c) SH4 and (d) SH5 samples after heating at 150 ^oC for 2 h, 8 h, 10 h, and 14 h, respectively.

Fig. 3. XRD patterns of (a) SH4 (w = 2.5), (b) SH7 (w = 3.0) and (c) SH8 (w = 3.5) solids where the solid products were prepared using precursor hydrogels with a molar composition of$1Al_2O_3:wP_2O_5:2.5[Bzm]_2O:180H_2O:0.47SiO_2$ heated at 150 °C for 10 h. The asterisks show the presence of cristobalite dense phase.

Fig. 4. (A) FESEM images and (B) particle size distributions of (a) SH4 (w = 2.5), (b) SH7 (w = 3.0) and (c) SH8 (w = 3.5) where the solid products were prepared using precursor hydrogels with a molar composition of $1Al_2O_3:wP_2O_5:2.5[Bzm]_2O:180H_2O:0.47SiO_2$ heated at 150 °C for 10 h.

Fig. 5. XRD patterns of (a) SH9 (x = 1.5), (b) SH10 (x = 2.0), (c) SH4 (x = 2.5) and (d) SH11 (x = 3.0) where the solid products were prepared using precursor hydrogels with a molar composition of$1Al_2O_3:xP_2O_5:x[Bzm]_2O:180H_2O:0.47SiO_2$ at 150 °C for 10 h.

Fig. 6. (A) FESEM images and (B) particle size distributions of (a) SH9 (x = 1.5), (b) SH10 (x = 2.0), (c) SH4 (x = 2.5) and (d) SH11 (x = 3.0) where the solid products were prepared using precursor hydrogels with a molar composition of $1Al_2O_3:xP_2O_5:x[Bzm]_2O:180H_2O:0.47SiO_2$ at 150 °C for 10 h.

Fig. 7. XRD patterns of (a) SH12 (y = 135), (b) SH4 (y = 180), (c) SH13 (y = 225) and (d) SH14 (y = 270) solid products which were prepared using precursor hydrogels containing $1Al_2O_3$:$2.5P_2O_5$:$2.5[Bzm]_2O$:yH_2O:$0.47SiO_2$ heated at 150 °C for 10 h. The asterisks show the presence of tridymite dense phase.

Fig. 8. (A) FESEM images and (B) particle size distributions of (a) SH12 (y = 135), (b) SH4 (y = 180), (c) SH13 (y = 225) and (d) SH14 (y = 270) solid products which were prepared using precursor hydrogels with a molar composition of $1Al_2O_3$:$2.5P_2O_5$:$2.5[Bzm]_2O$:yH_2O: $0.47SiO_2$ heated at 150 °C for 10 h.

Fig. 9. XRD patterns of (a) SH15 (z = 0), (b) SH16 (z = 0.23), (c) SH4 (z = 0.47) and (d) SH17 (y = 0.70) prepared with the precursor hydrogels containing $1Al_2O_3$:$2.5P_2O_5$:$2.5[Bzm]_2O$:$180H_2O$:$zSiO_2$ heated at 150 °C for 10 h.

Fig. 10. (A) FESEM images and (B) particle size distributions of (a) SH15 (z = 0), (b) SH16 (z = 0.23), (c) SH4 (z = 0.47) and (d) SH17 (y = 0.70) prepared using the hydrogels of $1Al_2O_3$:$2.5P_2O_5$:$2.5[Bzm]_2O$:$180H_2O$:$zSiO_2$ heated at 150 °C for 10 h.

Fig. 11. XRD patterns of (a) SH18, (b) SH19, (c) SH4 and (d) SH20 prepared with hydrogels of $1Al_2O_3$:$2.5P_2O_5$:$2.5[Bzm]_2O$:$180H_2O$:$0.47SiO_2$. The samples were heated at 100, 120, 150 and 200 °C for 10 h, respectively.

Fig. 12. (A) FESEM images and (B) particle size distributions of (a) SH18, (b) SH19, (c) SH4 and (d) SH20 prepared using hydrogels of $1Al_2O_3$:$2.5P_2O_5$:$2.5[Bzm]_2O$:$180H_2O$: $0.47SiO_2$. The samples were heated at 100, 120, 150 and 200 °C for 10 h, respectively.

Fig. 13. The hydrothermal crystallization pathway of SAPO-5 templating using [Bzm]OH.

Figures

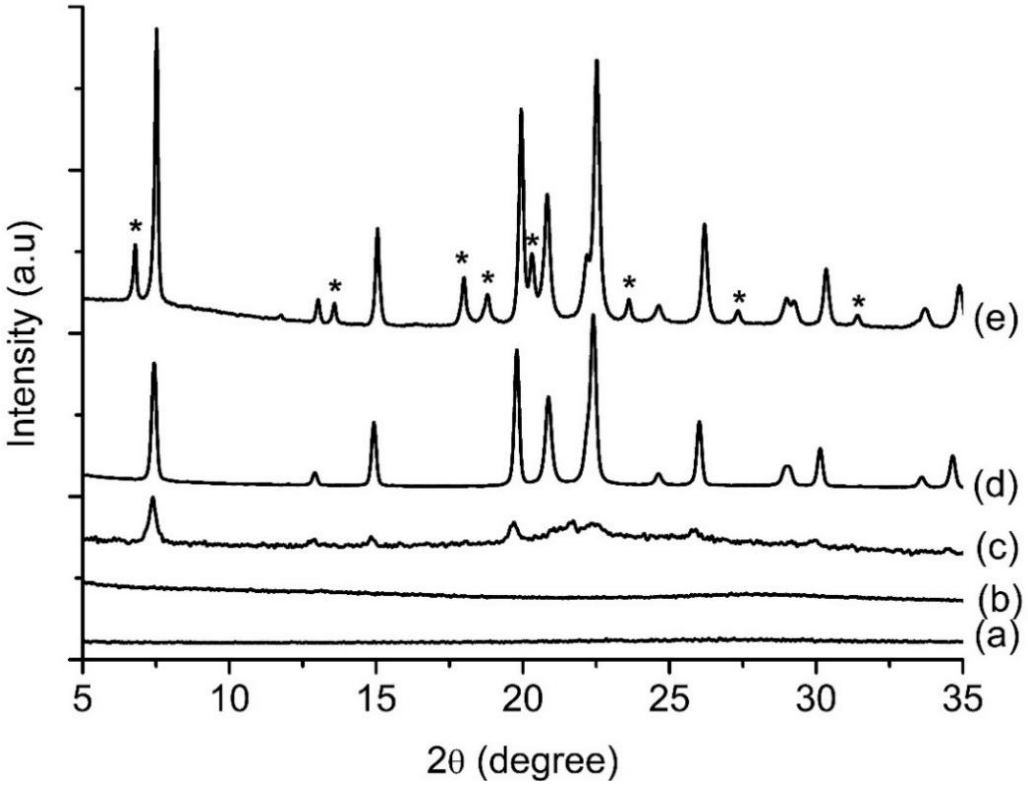

Fig. 1

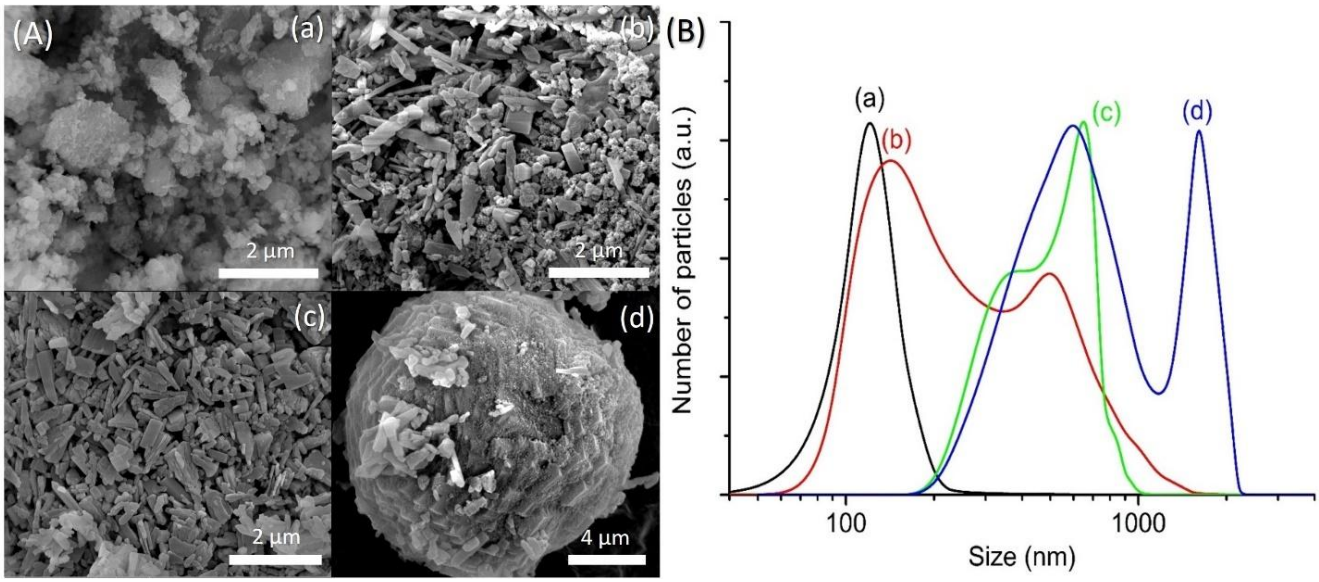
(A)
(a)
2 µm
(b)
2 µm
(c)
2 µm
(d)
4 µm
(B)
Number of particles (a.u.)
(a)
(b)
(c)
(d)
100
1000
Size (nm)

Fig. 2

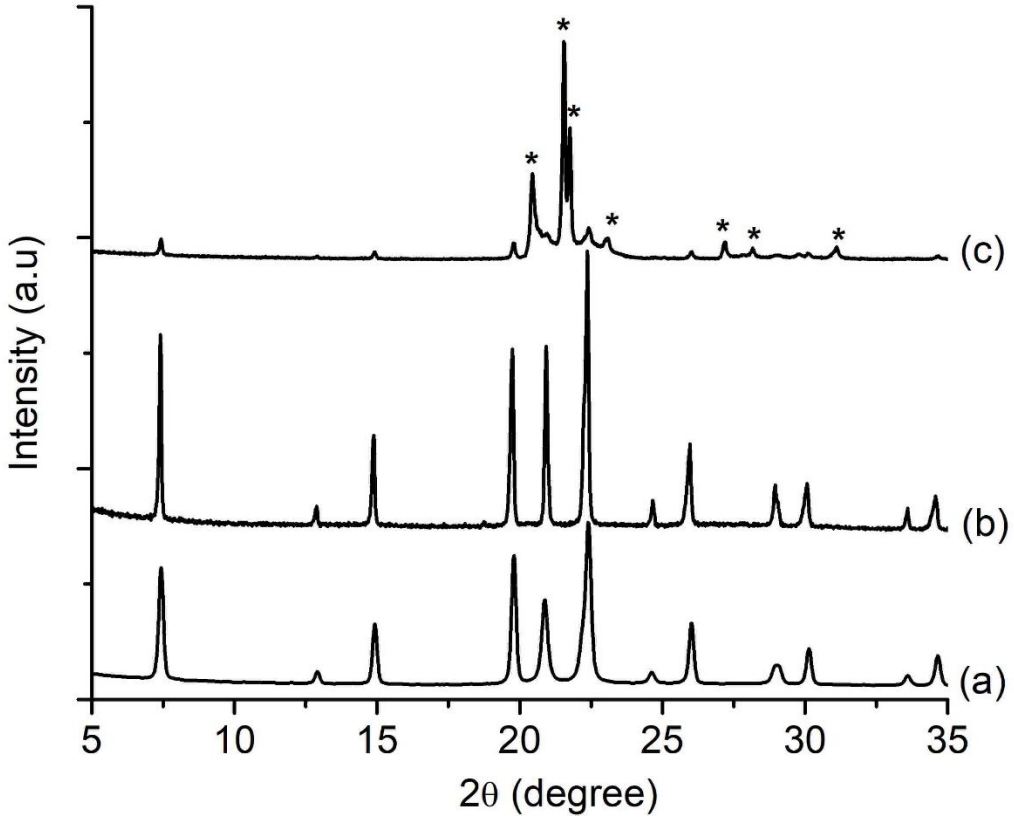

Fig. 3

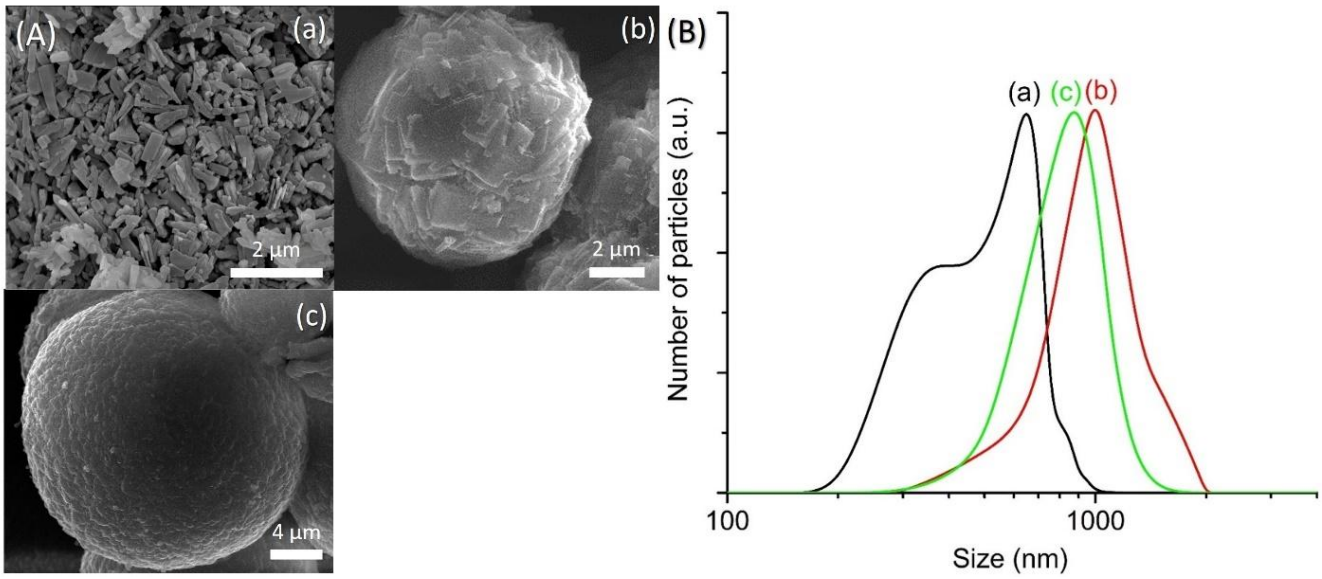

Fig. 4

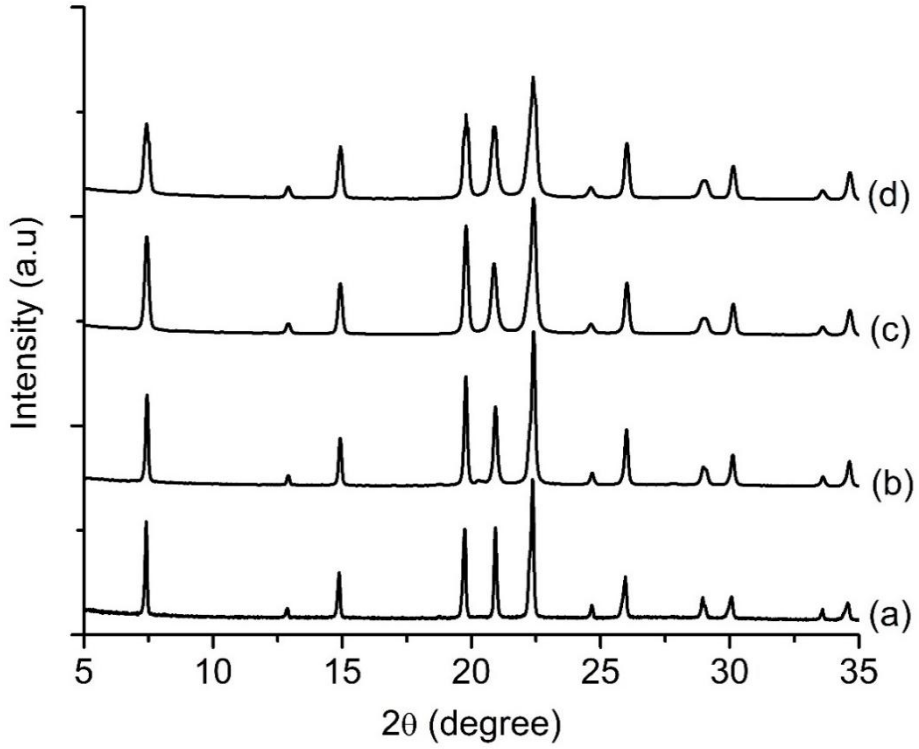

Fig. 5

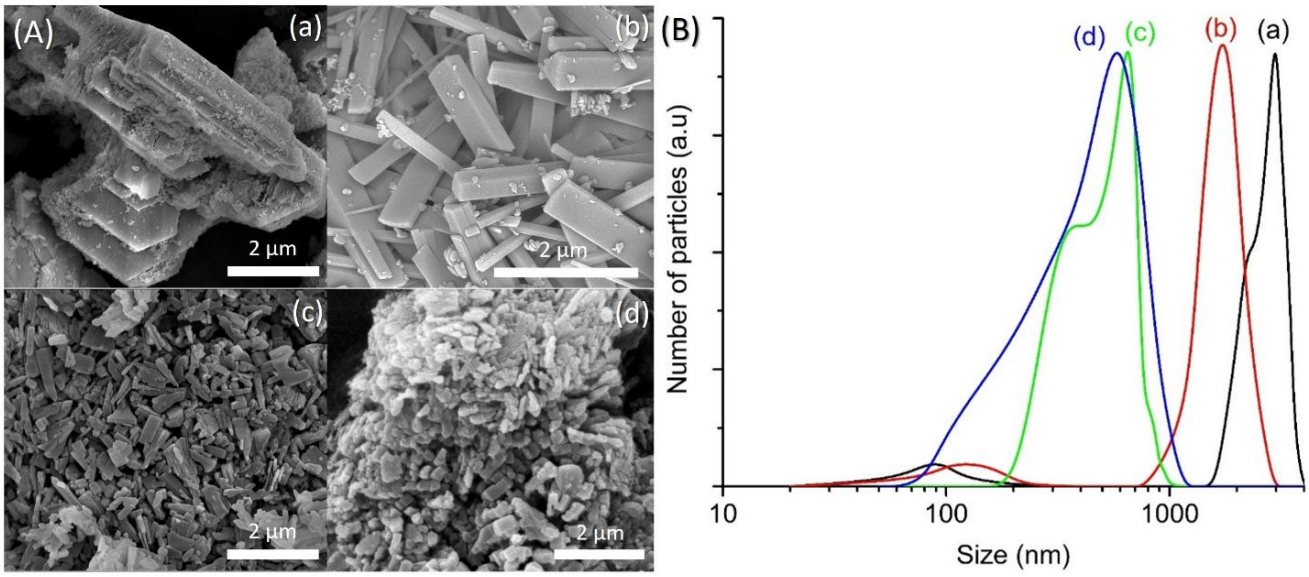
(A)
(a)
(b)
(c)
(d)
2 µm
2 µm
2 µm
2 µm
(B)
(d)
(c)
(b)
(a)
Number of particles (a.u)
10
100
1000
Size (nm)

Fig. 6

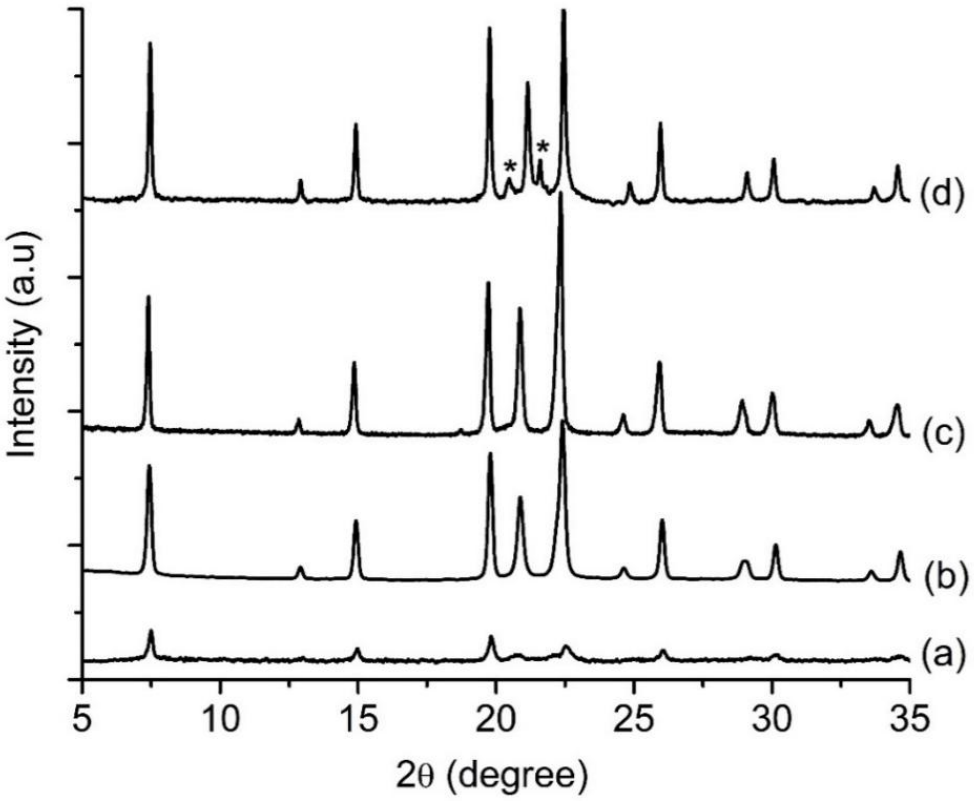

Fig. 7

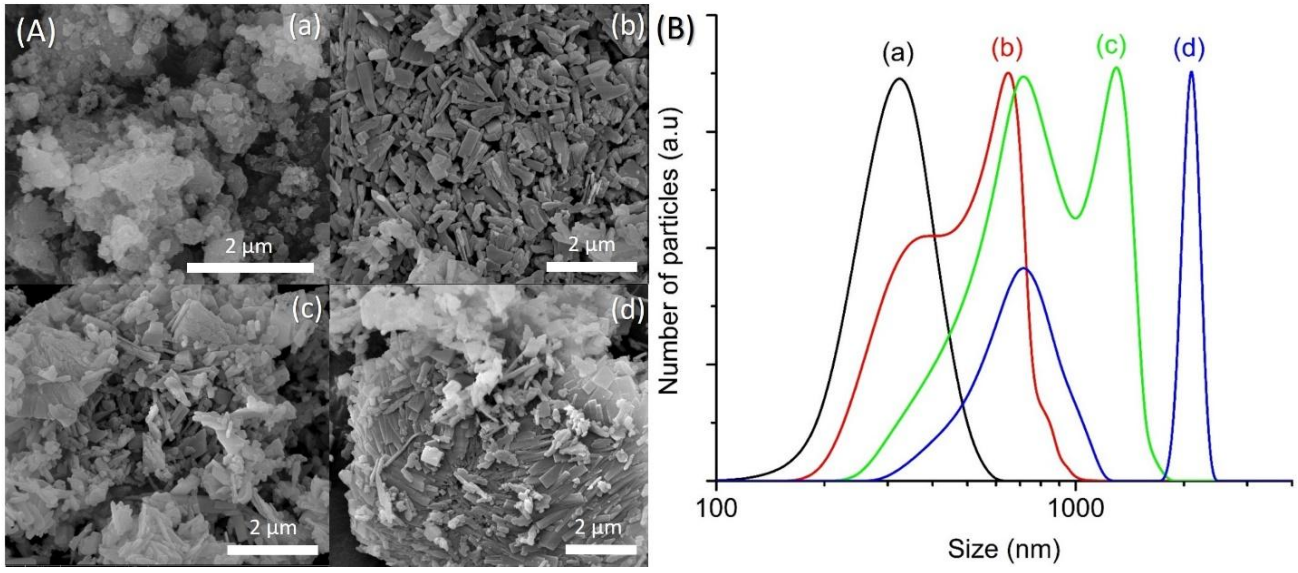
(A)
(a)
(b)
(c)
(d)
2 µm
2 µm
2 µm
2 µm
(B)
(a)
(b)
(c)
(d)
Number of particles (a.u)
100
1000
Size (nm)

Fig. 8

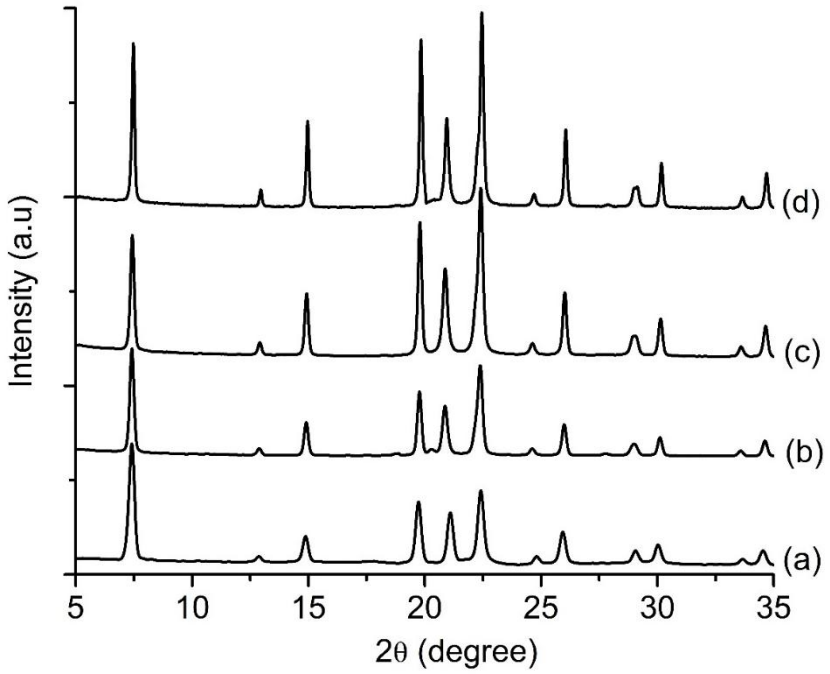

Fig. 9

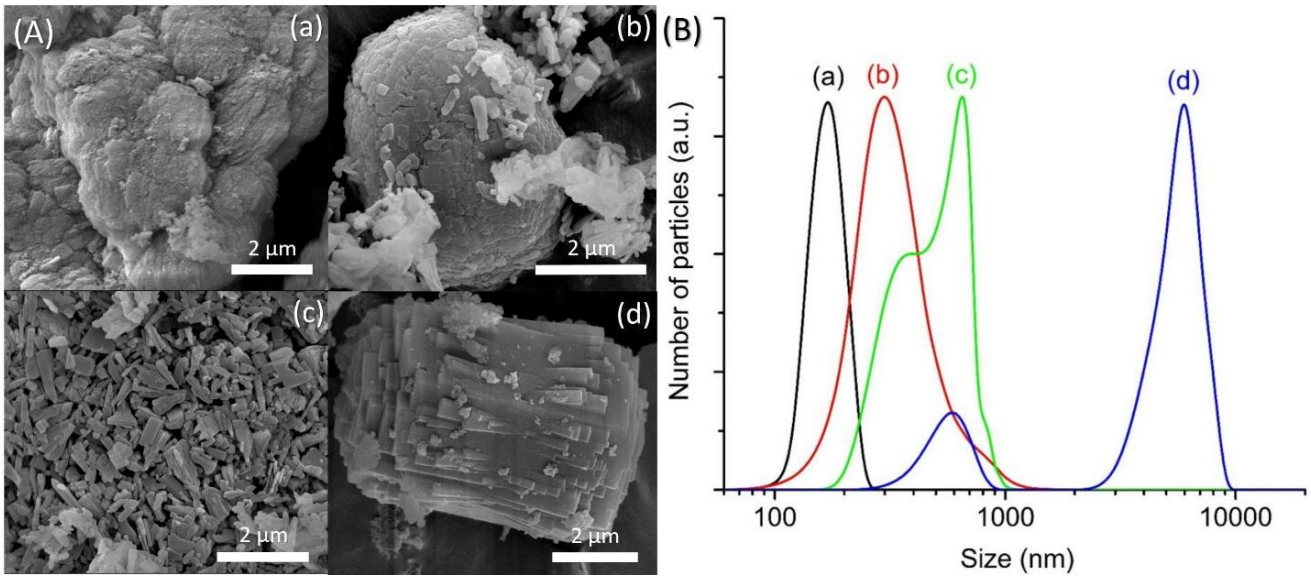
(A)
(a)
(b)
(c)
(d)
2 µm
2 µm
2 µm
2 µm
(B)
(a)
(b)
(c)
(d)
Number of particles (a.u.)
100
1000
10000
Size (nm)

Fig. 10

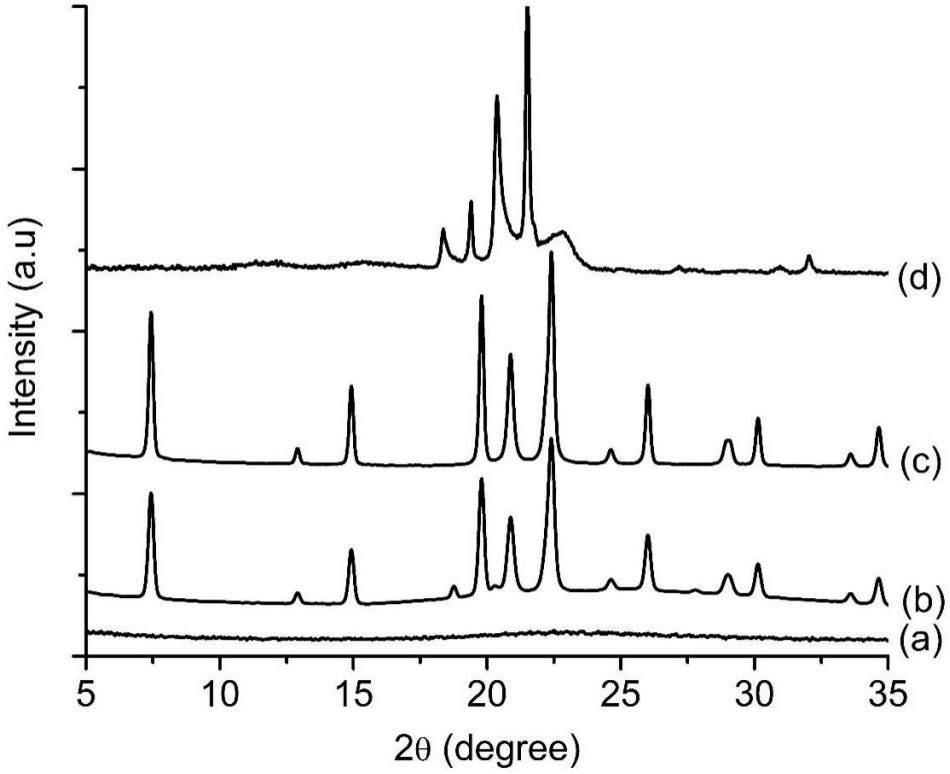

Fig. 11

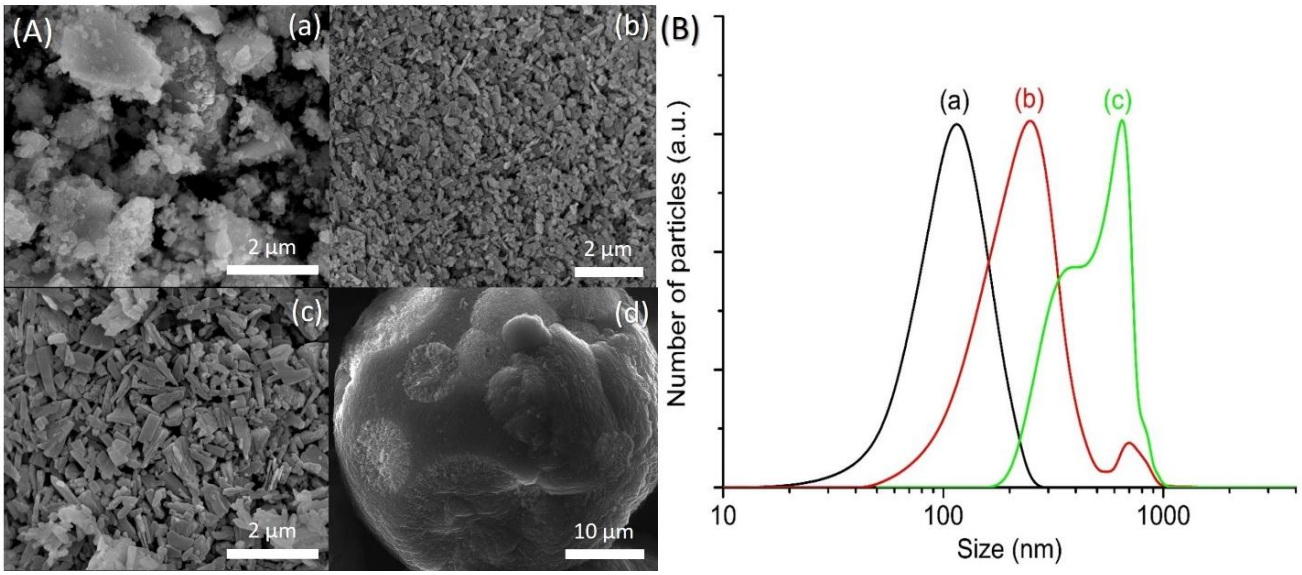
(A)
(a)
2 µm
(b)
2 µm
(c)
2 µm
(d)
10 µm
(B)
(a)
(b)
(c)
Number of particles (a.u.)
10
100
1000
Size (nm)

Fig. 12

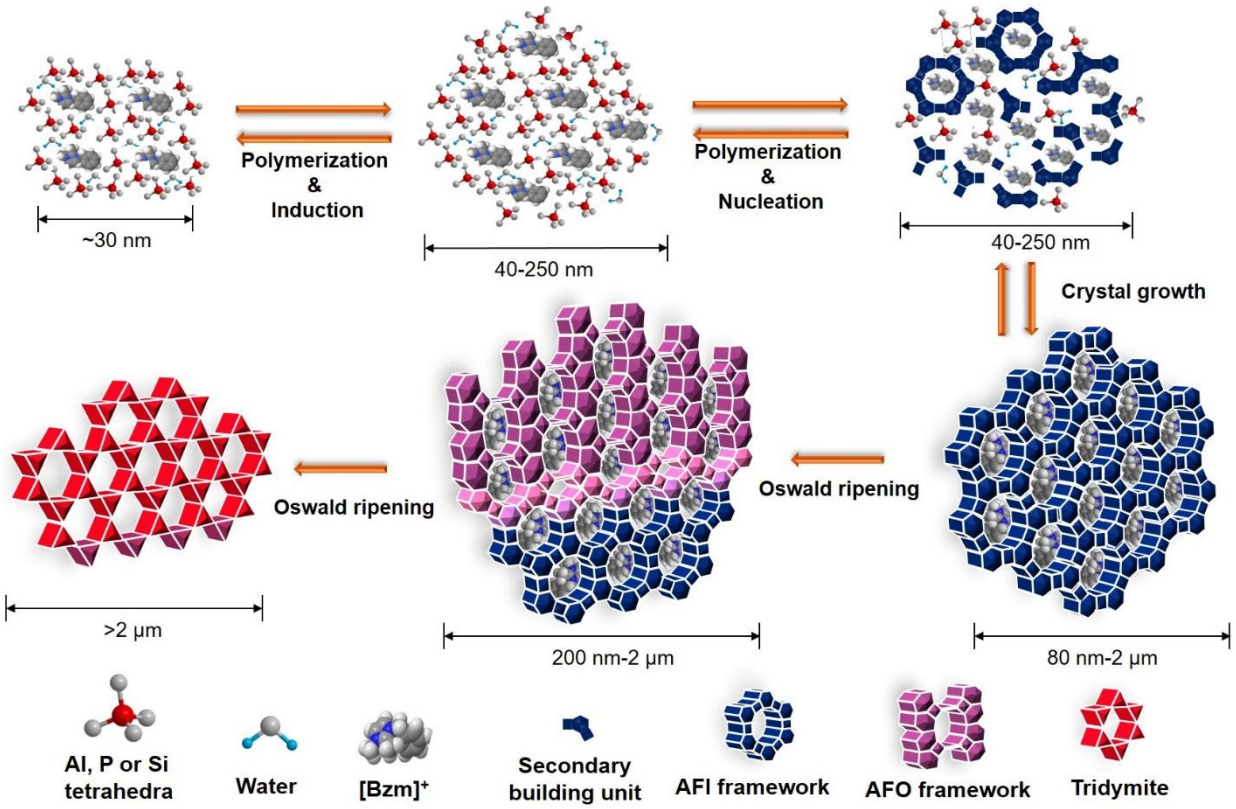
~30 nm
Polymerization & Induction
40-250 nm
Polymerization & Nucleation
40-250 nm
Crystal growth
>2 μm
Oswald ripening
200 nm-2 μm
Oswald ripening
80 nm-2 μm
Al, P or Si tetrahedra
Water
[Bzm]+
Secondary building unit
AFI framework
AFO framework
Tridymite

Fig. 13

Table

Table 1. Chemical composition and crystallization conditions of SH1-SH20 hydrogels together with the products obtained after altering the individual synthesis parameter.

Synthesis parameters	**Samples**	**Gel molar composition**					**T (℃)**	**t (h)**	**Products***
		Al_2O_3	**P_2O_5**	**$[Bzm]_2O$**	**SiO_2**	**H_2O**			
Time	SH1	1	2.5	2.5	0.47	180	150	2	Amor.
	SH2							4	Amor.
	SH3							8	Amor. + AFI
	SH4							10	AFI
	SH5							14	AFI + AFO
P_2O_5	SH6	1	2.0	2.5	0.47	180	150	10	No solid
	SH4		2.5						AFI
	SH7		3.0						AFI
	SH8		3.5						AFI + cristobalite
P_2O_5/ $[Bzm]_2O$	SH9	1	1.5	1.5	0.47	180	150	10	AFI
	SH10		2.0	2.0					AFI
	SH4		2.5	2.5					AFI
	SH11		3.0	3.0					AFI
H_2O	SH12	1	2.5	2.5	0.47	135	150	10	Amor. + AFI
	SH4					180			AFI
	SH13					225			AFI
	SH14					270			Tridymite

SiO_2	SH15	1	2.5	2.5	0	180	150	10	AFI (AlPO-5)
	SH16				0.23				AFI
	SH4				0.47				AFI
	SH17				0.7				AFI
Temperature	SH18	1	2.5	2.5	0.47	180	100	10	Amor.
	SH19						120		AFI
	SH4						150		AFI
	SH20						200		Tridymite

*Amor. = Amorphous; AFI = SAPO-5; AFO = SAPO-41